

A high-amplitude atmospheric inertia–gravity wave-induced meteotsunami in Lake Michigan

Eric J. Anderson & Greg E. Mann

Natural Hazards

ISSN 0921-030X

Nat Hazards

DOI 10.1007/s11069-020-04195-2



Your article is protected by copyright and all rights are held exclusively by This is a U.S. Government work and not under copyright protection in the US; foreign copyright protection may apply. This e-offprint is for personal use only and shall not be self-archived in electronic repositories. If you wish to self-archive your article, please use the accepted manuscript version for posting on your own website. You may further deposit the accepted manuscript version in any repository, provided it is only made publicly available 12 months after official publication or later and provided acknowledgement is given to the original source of publication and a link is inserted to the published article on Springer's website. The link must be accompanied by the following text: "The final publication is available at link.springer.com".



A high-amplitude atmospheric inertia–gravity wave-induced meteotsunami in Lake Michigan

Eric J. Anderson¹ · Greg E. Mann²

Received: 1 February 2020 / Accepted: 17 July 2020

© This is a U.S. Government work and not under copyright protection in the US; foreign copyright protection may apply 2020

Abstract

On Friday, April 13, 2018, a high-amplitude atmospheric inertia–gravity wave packet with surface pressure perturbations exceeding 10 mbar crossed the lake at a propagation speed that neared the long-wave gravity speed of the lake, likely producing Proudman resonance. A set of meteotsunami waves struck the shores near Ludington, Michigan, a coastal community along the sandy dunes of Lake Michigan. During the event, harbor walls were overtopped, damage occurred to shoreline homes and boat docks, and water intake pumps were impacted due to the large change in water level. To fully understand the generation of this event and the impacts to the coastal community, we have carried out atmospheric and hydrodynamic model simulations of the inertia–gravity and meteotsunami waves. Atmospheric simulation of the inertia–gravity waves was performed using a high-resolution model for the Great Lakes region that mimics the National Oceanic and Atmospheric Administration High-Resolution Rapid Refresh operational model. Surface meteorological conditions were supplied to the Lake Michigan-Huron Operational Forecast System, an operational model used for hydrodynamic forecast guidance. This is the first documented case of a meteotsunami generated by an atmospheric inertia–gravity wave in the Great Lakes, and it provides an evaluation of existing and proposed operational infrastructure as it pertains to meteotsunami forecasting in the USA.

Keywords Great Lakes · Meteotsunami · Gravity wave · Hydrodynamic · Lake Michigan

1 Introduction

Meteotsunamis are well documented in the Laurentian Great Lakes, with known hot spots in southern Lake Michigan and Lake Erie (Bechle et al. 2016). Several studies have advanced our understanding of meteotsunami generation and characteristics throughout the

✉ Eric J. Anderson
eric.j.anderson@noaa.gov

¹ Great Lakes Environmental Research Laboratory, Office of Oceanic and Atmospheric Research, National Oceanic and Atmospheric Administration, Ann Arbor, MI, USA

² Weather Forecast Office, National Weather Service, National Oceanic and Atmospheric Administration, White Lake, MI, USA

world (Nomitsu 1935; Hibiya and Kajiura 1982; Rabinovich and Monserrat 1996; Vilibić 2005; Monserrat et al. 2006; Rabinovich 2009; Haslett et al. 2009; Orlić et al. 2010; Cho et al. 2013; Šepić et al. 2015; Vilibić and Šepić 2017). In recent years, this understanding has been expanded to the Great Lakes to recreate historic events (Bechle and Wu 2014; Anderson et al. 2015; Linares et al. 2016, 2019) and develop a climatology of event occurrence for the region (Bechle et al. 2016). However, where globally meteotsunamis are commonly associated with atmospheric pressure disturbances, events in the Great Lakes region are often driven by more or less equally important gradients in atmospheric pressure and wind stress (Linares et al. 2016). The reason behind this may be that convective mesoscale weather systems with Proudman- or Greenspan-appropriate propagation speeds are common in the southern portion of the lakes, or that pressure disturbances in the region do not themselves suffice in the intensity or speed necessary to generate a meteotsunami wave. However, given that meteotsunami detection relies on coastal water level gauge placement and function, or at the very least eye witness reports, in conjunction with high-temporal-resolution meteorological observations, it may be that pressure-dominated meteotsunamis in the Great Lakes have not yet been observed or reported.

In this work, we document the first record of a high-amplitude atmospheric inertia–gravity (IG) meteotsunami in the Great Lakes (Fig. 1). In the morning of April 13, 2018, an IG wave packet was generated over the midwestern USA moving eastward toward Lake Michigan. As the series of three IG waves crossed over the lake, surface pressure disturbances approached 10 mbar ($\Delta P = 0.8$ mbar/min) accompanied by a single spike in wind speed associated with the second wave (Fig. 2). The system crossed over the narrowest reach of the lake, a width of 100 km, toward Ludington, Michigan, at a propagation speed of 27 m/s (Fig. 2). For this region of the lake where depths are greater than 100 m, gravity wave speeds are between 26 and 31 m/s, and thus, the storm speed was sufficient to induce a Proudman resonance (Proudman 1929). As a result, meteotsunami waves struck the Michigan coastline near Ludington in the early afternoon (15:30 GMT). The nearest coastal water level gauge to Ludington is located inside a harbor, where it recorded water level fluctuations up to 0.5 m (Fig. 2). Eyewitnesses at the beach observed the harbor break walls submerge below the lake surface with the incident waves and flood the shoreline and into the city streets. The National Weather Service

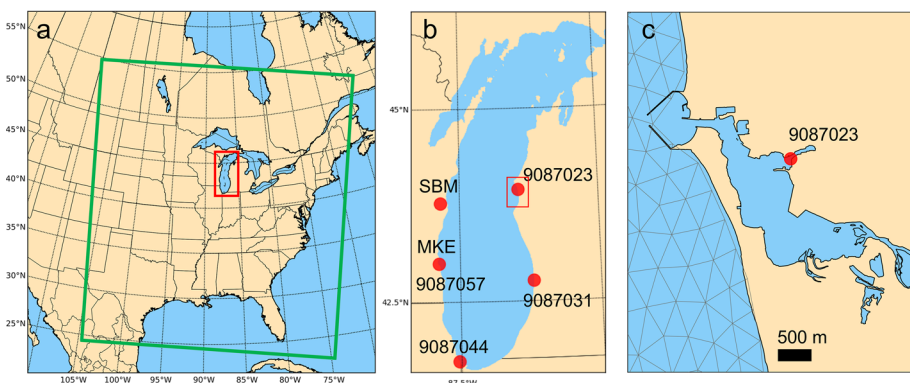


Fig. 1 **a** WRF domain (green box) over Great Lakes region and Lake Michigan inset (red box), **b** Lake Michigan with locations of NOS coastal water level gauges (9087023, 9087031, 9087044, and 9087057) and meteorological stations (SBM and MKE) with Ludington inset (red box), and **c** Ludington, Michigan harbor and estuary and NOS gauge location with LMHOFS model mesh overlay (gray)

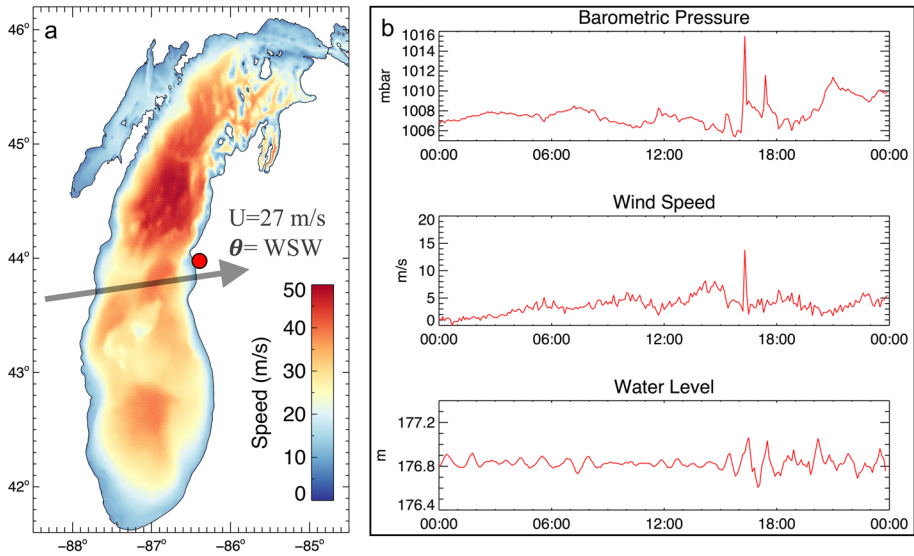


Fig. 2 **a** Long-wave speeds based on Lake Michigan depth and estimated storm propagation pathway and speed, **b** meteorological and water level observations from the Ludington, MI NOS gauge (9087023) on April 13, 2018 (shown in GMT)

(NWS) office in Grand Rapids, Michigan, received reports of water level fluctuations of 2 m along the coastline just outside of the harbor, where divers from a hydroelectric pumping plant were performing maintenance on a water intake at the time of the event. Shoreline damage to public docks and cottages was also reported. Fortunately, this event occurred much earlier than the typical recreational season, when it is not uncommon for a large number of beachgoers to be walking the harbor break walls or enjoying the water. For this reason, no injuries or fatalities were reported.

To fully understand the generation of this event and the impacts to the coastal community, we have carried out atmospheric and hydrodynamic model simulations of the IG and the resulting meteotsunami waves. Atmospheric simulation of the IG waves was achieved by using a high-resolution atmospheric model for the Great Lakes region, in which weather conditions are validated against coastal measurements and outputs provided to the hydrodynamic model. The hydrodynamic response was simulated using the National Oceanic and Atmospheric Administration (NOAA) Lake Michigan-Huron Operational Forecast System (LMHOFs; Anderson et al. 2018), which provides real-time nowcast and forecast guidance on water levels, currents, and temperatures to the public. The reconstructed meteotsunami event presents the first documentation of a high-amplitude pressure-induced meteotsunami in the Great Lakes, and it serves as a test of NOAA's operational infrastructure to capture the dangerous conditions and move toward the development of an operational meteotsunami warning system.

2 Methods

2.1 Meteorological and water level data

To document the atmospheric IG waves and validate atmospheric modeling of the event, meteorological data from five stations are obtained from the NOAA National Ocean Service (NOS) (stations 9087023, 9087031, and 9087044) and the Automated Surface Observing System (ASOS) [stations Milwaukee (MKE) and Sheboygan (SBM)] along with base reflectivity data from NEXRAD Weather Surveillance Radar are obtained. Observations of atmospheric pressure and wind speed and gust are reported every 6 min at the available stations. For evaluation of the coastal impact of the meteotsunami waves and for validation of the hydrodynamic model, 6-minute water level records from coastal NOS stations are acquired for four stations in Lake Michigan (9087023, 9087057, 9087031, 9087044; Fig. 1b). At 9087023, 9087031, and 9087044, both water levels and meteorological information are available. For water level station 9087057, the co-located MKE station is used to provide atmospheric conditions. Therefore, the only location without both water levels and meteorological conditions is SBM, which contains atmospheric pressure and wind measurements but does not have an associated water level gauge.

2.2 Atmospheric modeling

Simulation of the IG conditions during the meteotsunami event is performed using the Weather Research and Forecasting (WRF) model (Power et al. 2017). Two simulations were conducted on a modeling domain encompassing most of the Contiguous United States and southern Canada east of the Rocky Mountains using horizontal grid spacing of 15 km and 7 km, respectively, both using 51 vertical levels (Fig. 1a). Aside from the horizontal grid spacing, the WRF simulation construction is designed to mimic the existing NOAA High-Resolution Rapid Refresh (HRRRv3; Benjamin et al. 2016). Initial and hourly boundary conditions are prescribed from the NOAA Rapid Refresh (RAP), an operational weather forecast product on a 13-km grid (Benjamin et al. 2016). The model was initialized at 18:00 GMT April 12, 2018, to encapsulate the diurnal atmospheric convective cycle. Due to the high temporal frequency of the output, WRF surface conditions were output starting at 1:00 and 8:00 GMT on April 13 for the 15-km and 7-km simulations, respectively. Great Lakes surface temperature is prescribed by the NOAA Real-Time Global (RTG) 1/12th degree surface temperature analysis (Thiébaux et al. 2003). Output of surface meteorological conditions includes 10-m winds, 2-m surface atmospheric pressure, long-wave and short-wave radiation, 2-m relative humidity, and 2-m air temperature and are supplied to the hydrodynamic model at 2-min intervals.

2.3 Hydrodynamic modeling

The hydrodynamic response to the IG waves and generation of the meteotsunami waves is simulated by an experimental version of the NOAA LMHOFS (Anderson et al. 2018). The LMHOFS is a three-dimensional hydrodynamic model based on the Finite Volume Community Ocean Model (FVCOM; Chen et al. 2006). FVCOM simulates water levels, currents, and water temperature using an unstructured grid, free-surface, vertical sigma-coordinate system by solving the integral form of the governing equations. Implementations of FVCOM in the Great Lakes have been successfully employed for meteotsunami

investigations (Anderson et al. 2015) and other physical applications (Anderson and Schwab 2013, 2017; Ye et al. 2018). The LMHOFS implementation of FVCOM uses a horizontal unstructured grid (170,000 elements) that ranges from approximately 200 m nearshore to 2.5 km offshore with 21 uniform vertical sigma, terrain-following, layers. For this case, the FVCOM model is initialized from the NOAA LMHOFS on April 13, 2018, at hour 0 GMT. Surface meteorological forcing is supplied from the LMHOFS from 0 GMT to the start time of the two WRF cases described above (15-km and 7-km grids), with a computational time step of 2 s. Model output is produced every minute and compared to observed water level records from NOS coastal water stations. In many cases, including at the primary point of interest at Ludington, the NOS gauges are located inside harbors, coastal estuaries, or other infrastructure that is not resolved by the model domain (Fig. 1c). For model validation in these cases, the nearest model node to the gauge location is used for comparison with the observed water level record.

3 Results

3.1 Inertia-gravity waves

Radar reflectivity reveals the trajectory and timing of the weather disturbance on April 13, 2018 (Fig. 3). The pressure waves crossed the central region of the lake near 44° north latitude, moving west to east. According to high-pass-filtered atmospheric pressure data, only the SBM and Ludington (9087023) stations recorded the IG wave packet (Fig. 4). At the upwind station (SBM), the pressure record shows two IG waves passing at 14:18 and 15:24 GMT. Across the lake, the Ludington (9087023) stations record three IG waves at 15:18, 16:18, and 17:24 GMT. Recorded wind speeds at the stations were generally inconsequential, as is demonstrated below, with the exception of Ludington (9087023), which recorded a single high value (13.8 m/s) associated with the second pressure wave at 16:18 GMT. To calculate the approximate contribution of pressure and wind to the generated waves, we

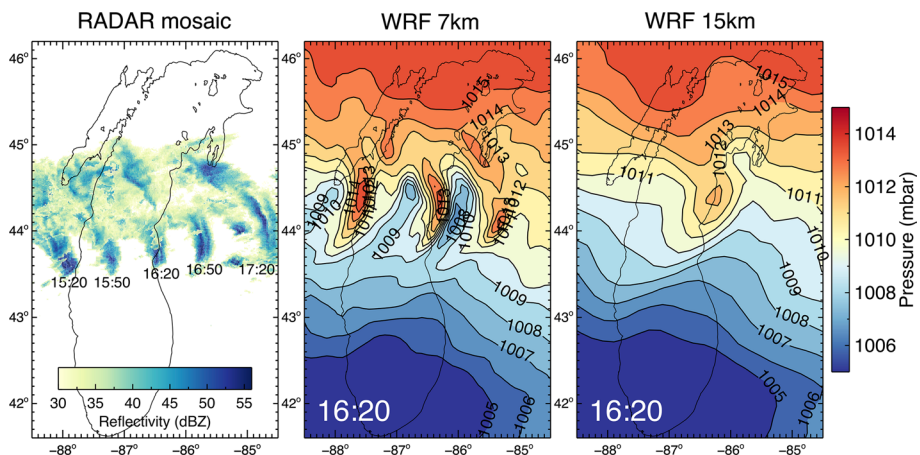


Fig. 3 (left) Radar reflectivity mosaic of inertia-gravity wave passage and snapshots from the 7-km (middle) and 15-km (right) WRF model simulations of the IG pressure wave packet at 16:20 GMT

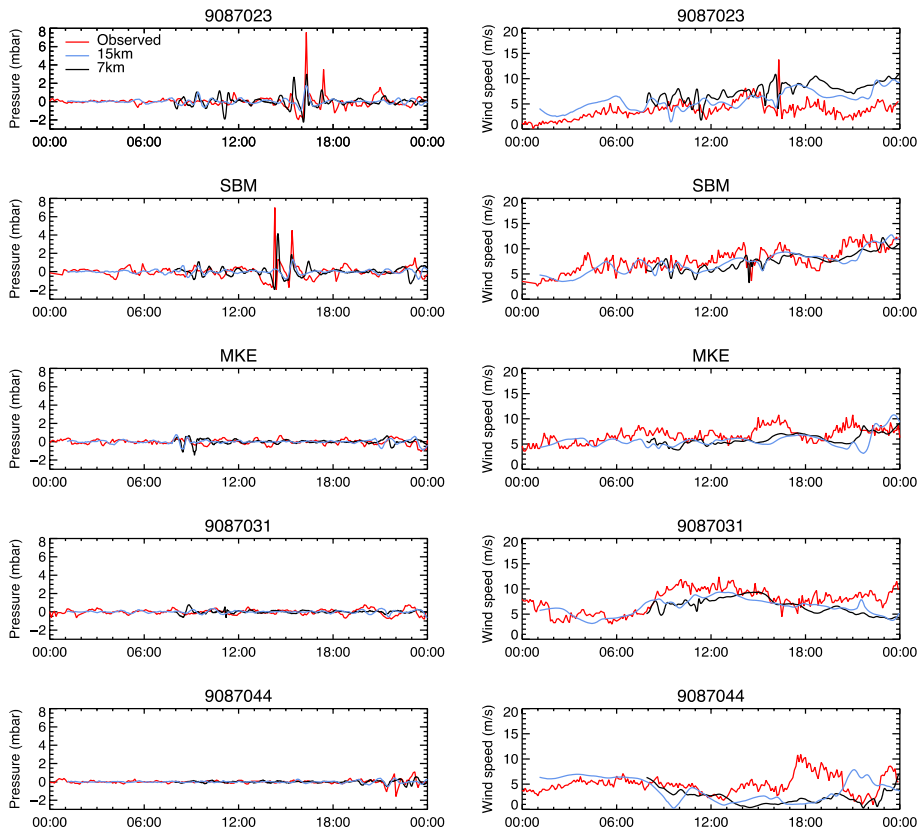


Fig. 4 High-pass-filtered atmospheric pressure (left column) and wind speed (right column) at coastal meteorological stations for observed values (red) and the 15-km (blue) and 7-km (black) resolution WRF simulations on April 13, 2018 (time in GMT)

can assume a linear and barotropic solution at constant depth, such that the shallow water equations can be written as

$$\frac{\partial u}{\partial t} + g \frac{\partial \eta}{\partial x} = \frac{1}{\rho} \left[-\frac{\partial P}{\partial x} + \frac{\tau}{D} \right] \quad (1)$$

where u is velocity, t is time, g is the gravitational constant, η is the surface displacement, x is the coordinate of the IG propagation, ρ is the density of water, P is the atmospheric surface pressure, τ is the wind stress, and D is the average lake depth along x . Wind stress can be calculated using the quadratic drag formulation,

$$\tau = \rho_a C_D |W| (w_x, w_y) \quad (2)$$

where ρ_a is the density of air, W is the wind speed, w_x and w_y are wind velocity components, and C_D is the drag coefficient calculated from a linear relationship with wind speed (Smith 1980).

Using the sole spike in wind speed at Ludington (9087023), which coincides with the second pressure wave, a wind speed of 13.8 m/s and average depth of 100 m gives

$\tau/\rho D = 3.58 \times 10^{-6} \text{ m/s}^2$. For the IG wave contribution, a pressure change of 9.7 mbar over 12 min and storm propagation speed, U , of 27 m/s gives $\Delta P/\rho \Delta x = 4.99 \times 10^{-5} \text{ m/s}^2$. Therefore, the overall contribution to water surface displacement from pressure is approximately 93%, whereas the contribution from wind stress is 7%.

The WRF simulations of the event reveal the large amplitude IG wave packet as they traverse Lake Michigan (Fig. 3). Both the 15-km and 7-km simulations are able to resolve aspects of the IG system, which does not require the fine resolution necessary for more convective systems that typically produce meteotsunamis in the Great Lakes (Anderson et al. 2015). However, notable differences exist between the two simulations (Figs. 3, 4). Namely, the 15-km simulation produces just a single large pressure wave that is timed with the second observed wave at SBM and Ludington (9087023), failing to resolve the leading IG wave at both stations and the trailing wave at Ludington. However, the 7-km WRF simulation represents the packet of IG waves appreciably better than the coarser 15-km configuration—with the timing of the leading, peak, and trailing waves being within minutes of the observed pressure signals. In both cases, the simulated amplitude of the IG waves is substantially dampened compared to observations at these locations, with the exception of the first wave at Ludington for the 7-km case. The 7-km simulation wave amplitudes for the second and third waves at Ludington are nearly half of the observed conditions; however, a sharp change in pressure is still achieved, reaching 0.42 mbar/min and far exceeding common empirical thresholds for meteotsunami formation in the Great Lakes (Linares et al. 2016). At the remaining coastal stations (MKE, 9087031, and 9087044), both simulations track measured pressure values and confirm the absence of the IG packet in the southern region of the lake. In regard to wind speeds, both produce the lack of increased winds at SBM, MKE, and 9087031, but fail to resolve the single spike in wind at the Ludington (9087023) station at 16:18 GMT and a prolonged rise measured at 9087044. However, since the estimated contribution of wind stress to the observed wave height is 7%, the inability of the model to capture the wind jump at Ludington should not be costly to the predicted wave heights.

3.2 Meteotsunami waves

Using an experimental version of the FVCOM-based LMHOFS model, the hydrodynamic response to the IG waves was evaluated using both 7- and 15-km meteorological simulations. For the first time, the FVCOM model provides us with a spatiotemporal representation of the generation of the April 13 meteotsunami event (Fig. 5). With IG propagation speeds near the water gravity wave speed, Proudman resonance led to the generation of meteotsunami waves in the lake. Even for the short fetch at this location, the high-amplitude nature of the IG waves resulted in significant wave heights. Associated with the first IG wave, a long wave was produced over the lake that traveled eastward toward Ludington. The bathymetric variation in the lake caused wave refraction which resulted in an anti-cyclonic turn over the middle of the lake (Fig. 5). The first wave struck the coast near Ludington at 15:24 GMT (Figs. 5b, 6), resulting in the creation of trapped edge waves that traveled north and south along the coasts as well as reflected waves that traveled back to the west coast of the lake. Shortly after, the second IG wave produced the largest meteotsunami wave of the event and took a similar path (Fig. 5c, d), striking the shore at 16:30 GMT, and again producing edge and reflected waves. Finally, a third wave followed, incident with the third IG wave (Fig. 5f), and hit the coast near Ludington at 17:30 GMT. Following the IG-associated waves, another large wave was detected at Ludington at 20:12 GMT (Fig. 5);

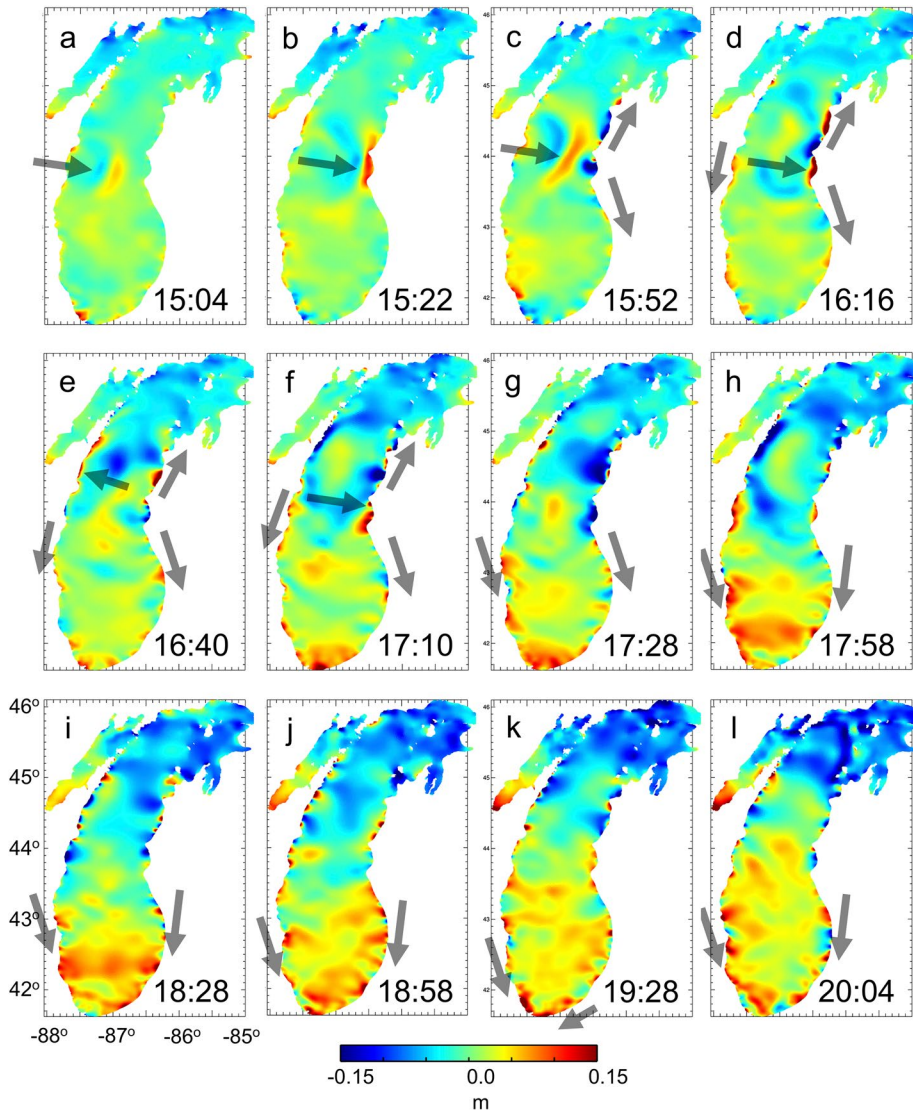


Fig. 5 FVCOM hydrodynamic response using 7-km WRF forcing (times shown in GMT). Arrows depict traveling long waves and coastally trapped edge waves

however, there is no apparent atmospheric driver, suggesting that this is likely a reflected wave from one of the earlier events. Given the zonal distance across this region of the lake is approximately 100 km (or 200 km roundtrip), wave speeds between 20 and 30 m/s would place the wave of origin at Ludington between 17:26 and 18:21 GMT, suggesting that the third meteotsunami event (17:30) may be the culprit.

Given that the two WRF simulations yielded significantly different IG structures, the resulting FVCOM simulations produced equally different representations of the meteotsunami event. Under the 7-km WRF results, FVCOM produced water level fluctuations at

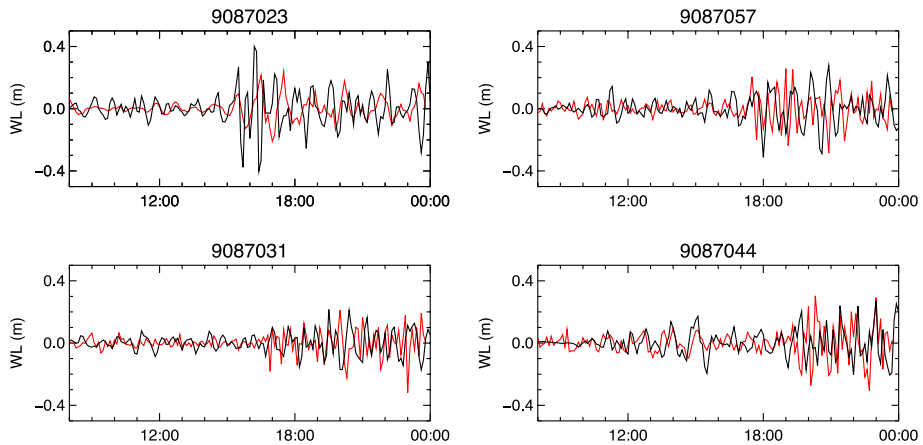


Fig. 6 High-pass-filtered observed (red) and modeled (black) water levels at coastal NOS stations using the 7-km meteorological forcing (time in GMT, April 13, 2018)

the Ludington gauge that roughly match the timing of the first wave (Fig. 6). The modeled wave amplitude is more than double the observed water level rise at the gauge. Similarly, the second and third waves arrive at Ludington slightly earlier than the observed waves, where again the amplitude of the second wave far exceeds that of the observed; however, the amplitude of the third wave agrees well with the gauge observation. It is important to note that the gauge is located inside a drowned river mouth estuary and behind harbor break walls. These conditions will certainly impact the amplitude and timing of waves as compared to the open lake given the differences in resonant characteristics of the estuary. Given that the model does not resolve these harbor areas, it is not surprising that these differences in wave response exist. However, as noted earlier, eyewitness reports suggest water level fluctuations outside the harbor breakwalls may have been as high as 2 m. Although the accuracy of these reports cannot be confirmed, it may provide an explanation of why the model water level fluctuations approach 0.8 m in this area, and suggests that if the atmospheric forcing had provided a larger amplitude pressure jump as observed at Ludington, it may have approached the eyewitness reported level. Higher-frequency waves are also produced by the model than what is observed, though these differences may be related to similar reasoning related to gauge location. Overall, three primary meteotsunami waves can be seen from the 7-km model results that correspond to those observed in the water level record. Similar to the observed record at 20:12 GMT, a large wave occurs more than 2 h after the IG wave packet has passed. The modeled wave arrives before the observed fluctuation (19:40 GMT), which is likely due to the timing issues noted above, but the amplitude agrees well with the observations. Snapshots from the model simulation reinforce the idea that this wave was likely reflected from the 17:30 Ludington wave (Fig. 5).

Under the 15-km WRF forcing with a single IG wave, only one large meteotsunami wave is produced (Fig. 7). The wave amplitude at Ludington is dampened compared to the 7-km case and arrives roughly halfway between the observed first and second waves. The amplitude of the wave nearly matches the observed height of the second wave; however, given that the estuary which houses the gauge location is not included in the model, this may be coincidental. Also, notably absent in this simulation is the observed wave that occurred at 20:12 GMT. Without the IG wave packet, and more precisely without the third

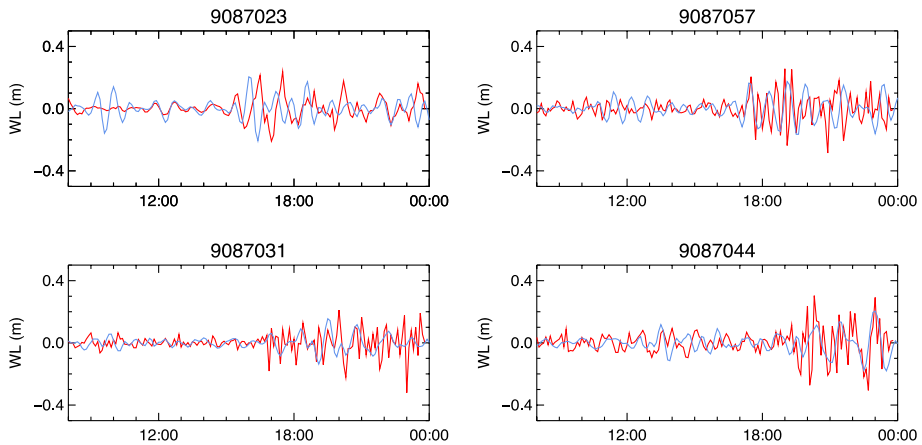


Fig. 7 High-pass-filtered observed (red) and modeled (blue) water levels at coastal NOS stations using the 15-km meteorological forcing (time in GMT, April 13, 2018)

IG wave-induced meteotsunami, there is no reflected wave that occurs near 20:00. This difference between the 7- and 15-km simulations is further evidence that the 20:12 GMT wave was reflected from the 17:30 Ludington wave.

At nearby coastal water level gauges (9087031, 9087057, and 9087044), the meteotsunami waves arise as a result of reflected long waves and trapped edge waves. At the 9087031 gauge, water level fluctuations within the tsunami frequency band are first observed at 16:54 GMT (Fig. 6) with a wave period between 18 and 24 min. Analysis of the Ludington results suggested that edge waves were produced from the incident meteotsunami waves that traveled south along the coast toward 9087031 (Fig. 5c, d, e). Coastally trapped edge waves travel at speeds given by the dispersion relationship,

$$C_{\text{edge}} = \frac{gT \tan [\beta(2n + 1)]}{2\pi} \quad (3)$$

where T is wave period, β is the bathymetric slope, and n is the mode number (taken as zero for the analysis below). For a slope of 0.011, C_{edge} would be 25 m/s. Using the distance between the Ludington and 9087031 gauges, 140 km, and the wave arrival times, the approximate observed wave speed is 26 m/s, suggesting that edge waves were responsible for the fluctuations at 9087031. Both model simulations capture the onset of the edge waves near 17:00 GMT, due to a wave train related to the incidence waves at Ludington, which continue for the remainder of the day (Figs. 6, 7).

On the west side of the lake, the next coastal water level gauge to be impacted is 9087057, where water level fluctuations begin at 17:30 GMT with a period near 24 min. The source of these waves likely stems from direct reflection and refraction of the Ludington waves or a combination of reflected long waves and trapped edge waves. For a straight line distance between Ludington and 9087057 of 150 km, reflections of the first (15:24 GMT) and second (16:30 GMT) Ludington waves would suggest long wave speeds of 20 and 42 m/s, approximately. However, the calculated long wave speeds in this region are closer to 30 m/s (Fig. 2a). Thus, it may be a combination of a reflected first wave that travels westward across the lake and then produces edge waves that travel south toward 9087057. In this case, a westward reflected first wave would impact the western shore

around 16:19 GMT (given a westward distance of 100 km and wave speed of 30 m/s) and travel south for 100 km to reach the 9087057 gauge at 17:30 GMT. This would require edge wave speeds near 23 m/s. We can verify this using (3), where for a bathymetric slope ranging between 0.00625 and 0.0125, calculated edge wave speeds fall between 14 and 28 m/s. With the 7-km forcing, the FVCOM model supports this notion, where a reflected wave appears on the western shore near 16:16 (Fig. 5d) and then a series of edge waves travel along the coast, reaching 9087057 after 17:30 GMT (Fig. 5e–h). A time series comparison between the model and gauge record shows a slight time mismatch, but otherwise agrees with the onset and duration of the wave conditions (Fig. 6). The 15-km forced FVCOM model produces a similar picture of edge wave arrival with slightly better timing than the high-resolution case (Fig. 7). Following this initial onset, it also appears that the second Ludington wave (16:30 GMT) has a similar effect to that of the first, where reflection westward toward the coast and a south-moving edge wave train reaches the gauge at 19:00 GMT, marked by an increase in observed wave amplitude.

Finally, the meteotsunami waves reach 9087044 at the southern edge of the lake at 19:42 GMT. Following the analyses for 9087031 and 9087057 above, the edge waves produced from the first Ludington wave proceeded southward along both shorelines (Fig. 5). If the edge waves that passed 9087031 at 16:54 GMT continued onto 9087044, a shoreline distance of 180 km would yield an average edge wave speed of 18 m/s. This is close to the edge wave speed for the first mode with an average bathymetric slope of 0.0030, where (3) yields 20 m/s. Along the west coast of the lake, a similar calculation is made, where the distance from 9087057 to 9087044 is 150 km. For the edge waves that passed 9087057 at 17:30 GMT, this distance would require average edge wave speeds of 19 m/s. Using (3), a calculated edge wave speed confirms a similar speed with a value of 17 m/s, using an average slope of 0.0025. The FVCOM model using the 7-km forcing confirms the approach of trapped edge waves from both directions toward 9087044 (Fig. 5), where the wave arrival time occurs just before 20:00 GMT and continues for the remainder of the day (Fig. 6). Similarly, the 15-km forced model shows the edge wave arrival near 19:42 GMT with a magnitude that matches the gauge value, though the wave period is longer than the observed (Fig. 7).

4 Discussion

The April 2018 Ludington event in Lake Michigan represents the first documented high-amplitude pressure-driven meteotsunami in the Great Lakes. Significant work in recent years has sought to understand meteotsunami generation mechanisms in the Great Lakes and around the world. What is unique to the Great Lakes is that notable historic meteotsunami events have been driven by equally important wind stress and atmospheric pressure perturbations, unlike the pressure-dominated events found elsewhere on the coastal ocean. The majority of the events in the lakes are driven by convective weather, which is prone to occur along southern Lake Michigan and Lake Erie, the locations of the most known events. However, the prediction of convective mesoscale systems on the scale required to generate meteotsunami waves in the lakes is difficult with existing numerical weather prediction models. Thus, the development of a meteotsunami warning system for the USA has looked toward a detection-based approach by leveraging tsunami-detection buoys (e.g., DART system; Spillane et al. 2008). Although useful along the ocean coasts, no buoys of

this type are deployed in the Great Lakes. Therefore, a different approach may be required in the Great Lakes in order to provide advanced warning of meteotsunami waves.

In this study, we investigate a high-amplitude IG wave-driven meteotsunami and test numerical models that are similar to those used in NOAA operations in order to test their ability to resolve IG-generated meteotsunami waves. IG wave events may not require the same horizontal resolution necessary in convective events, and thus this work serves as a test of NOAA's operational capability in forecasting a subset of meteotsunami conditions. We find that even under coarse resolution in the atmospheric model, high-temporal-resolution output can produce adequate IG wave structure such that existing operational hydrodynamic models will generate meteotsunami conditions. The limitation here is simply that the temporal resolution must be able to adequately capture the IG propagation (e.g., <5 min output). Given the limited amount of surface information needed from weather models to drive operational hydrodynamic models, this frequency of meteorological output may be possible in an uncoupled real-time system.

In both cases tested here, the approximate timing of meteotsunami arrival at several coastal stations agreed with observations from gauged water levels. Higher spatial resolution may have produced more accurate IG wave packets and thus more realistic number and amplitude of meteotsunami waves, though both tests would be able to provide the information to the public for advanced warning of dangerous nearshore conditions and flooding potential. To resolve the nearshore dynamics in further detail and provide accurate inundation maps, including the transfer of the wave signal into the harbor/estuary, a higher-resolution hydrodynamic model is required that resolves these features and accurately captures the dynamics related to wetting and drying and wave run-up, and should be the goal of future work.

Overall, models tested here provide an evaluation of NOAA's existing operations in predicting IG-driven meteotsunami events. Although these types of pressure-dominated events are not the most common driver of meteotsunamis in the Great Lakes, without a meteotsunami detection system, this may provide the best opportunity to provide advanced warning to the public for these types of conditions.

Acknowledgements This is GLERL publication number 1956.

Author contributions EA and GM conceived of and wrote the manuscript. GM completed the atmospheric simulations. EA completed the hydrodynamic simulations. EA and GM analyzed model results.

Data availability Water level and meteorological data are available from <https://tidesandcurrents.noaa.gov/>. LMHOFS model input and output are available from <https://opendap.co-ops.nos.noaa.gov/thredds/catalog.html>.

Code availability FVCOM code is available from <http://fvcom.smast.umassd.edu/FVCOM/Source/code.htm>. WRF code is available from <https://www2.mmm.ucar.edu/wrf/users/downloads.html>.

Compliance with ethical standards

Conflict of interest The authors declare that they have no conflict of interest.

References

- Anderson EJ, Schwab DJ (2013) Predicting the oscillating bi-directional exchange flow in the Straits of Mackinac. *J Great Lakes Res* 39(4):66671

- Anderson EJ, Schwab DJ (2017) Meteorological influence on summertime baroclinic exchange in the Straits of Mackinac. *J Geophys Res Oceans* 122(3):2171–2182
- Anderson EJ, Bechle AJ, Wu CH, Schwab DJ, Mann GE, Lombardy KA (2015) Reconstruction of a meteotsunami in Lake Erie on 27 May 2012: Roles of atmospheric conditions on hydrodynamic response in enclosed basins. *J Geophys Res Oceans* 120:8020–8038. <https://doi.org/10.1002/2015JC010883>
- Anderson EJ, Fujisaki-Manome A, Kessler J, Lang GA, Chu PY, Kelley JGW, Chen Y, Wang J (2018) Ice forecasting in the next-generation Great Lakes Operational Forecast System (GLOFS). *J Mar Sci Eng* 6(4):123. <https://doi.org/10.3390/jmse6040123>
- Bechle AJ, Wu CH (2014) The Lake Michigan meteotsunamis of 1954 revisited. *Nat Hazards* 74:155–177. <https://doi.org/10.1007/s11069-014-1193-5>
- Bechle AJ, Wu CH, Kristovich DAR, Anderson EJ, Schwab DJ, Rabinovich AB (2016) Meteotsunamis in the Laurentian Great Lakes. *Sci Rep* 6:37832. <https://doi.org/10.1038/srep37832>
- Benjamin SG, Weygandt SS, Brown JM, Hu M, Alexander CR, Smirnova TG, Olson JB, James EP, Dorell DC, Greg GA, Lin H, Peckham SE, Smith TL, Moninger WR, Kenyon JS, Manikin GS (2016) A North American hourly assimilation and model forecast cycle: the rapid refresh. *Mon Weather Rev* 144:1669–1694. <https://doi.org/10.1175/MWR-D-15-0242.1>
- Chen C, Beardsley RC, Cowles G (2006) An unstructured grid, finite volume coastal ocean model (FVCOM) system. *Oceanography* 19:78–89
- Cho KH, Choi JY, Park KS, Hyun SK, Oh Y, Park JY (2013) A synoptic study on tsunami-like sea level oscillations along the west coast of Korea using an unstructured-grid ocean model. *J Coast Res* 65:678–683
- Haslett SK, Mellor HE, Bryant EA (2009) Meteotsunami hazard associated with summer thunderstorms in the United Kingdom. *Phys Chem Earth* 34:1016–1022
- Hibiya T, Kajiura K (1982) Origin of the Abiki phenomenon (a kind of seiche) in Nagasaki Bay. *J Oceanogr Soc Jpn* 38:172–182
- Linares A, Bechle AJ, Wu CH (2016) Characterization and assessment of the meteotsunami hazard in northern Lake Michigan. *J Geophys Res Oceans* 121(9):7141–7158. <https://doi.org/10.1002/2016JC011979>
- Linares A, Wu CH, Bechle AJ, Anderson EJ, Kristovich DAR (2019) Unexpected rip currents induced by a meteotsunami. *Sci Rep* 9:2105. <https://doi.org/10.1038/s41598-019-38716-2>
- Montserrat S, Vilibić I, Rabinovich AB (2006) Meteotsunamis: Atmospherically induced destructive ocean waves in the tsunami frequency band. *Nat Hazards Earth Syst Sci* 6(6):1035–1051
- Nomitsu T (1935) A theory of tsunamis and seiches produced by wind and barometric gradient. *Mem Coll Sci Kyoto Imp Univ* 18:201–214
- Orlić M, Belušić D, Janeković I, Pasarić M (2010) Fresh evidence relating the great Adriatic surge of 21 June 1978 to mesoscale atmospheric forcing. *J Geophys Res* 115:C06011
- Power JG et al (2017) The weather research and forecasting model: overview, system efforts, and future directions. *Bull Am Meteorol Soc* 98:1717–1737
- Proudman J (1929) The effects on the sea of changes in atmospheric pressure. *Geophys Suppl Mon Not R Astron Soc* 2(4):197–209
- Rabinovich AB (2009) Seiches and harbor oscillations. In: Kim YC (ed) *Handbook of coastal and ocean engineering*. World Sci, Singapore, pp 193–236
- Rabinovich AB, Monserrat S (1996) Meteorological tsunamis near the Balearic and Kuril Islands: descriptive and statistical analysis. *Nat Hazards* 13:55–90
- Šepić J, Vilibić I, Fine I (2015) Northern Adriatic meteorological tsunamis: assessment of their potential through ocean modeling experiment. *J Geophys Res Oceans* 120:2993–3010
- Smith SD (1980) Wind stress and heat flux over the ocean in gale force winds. *J Phys Oceanogr* 10:709–726
- Spillane MC, Gica E, Titov EE, Mofjeld HO (2008) Tsunami network design for the U.S. DART arrays in the Pacific and Atlantic Oceans. NOAA Technical Memorandum OAR PMEL-143
- Thiébaux J, Rogers E, Wang W, Katz B (2003) A new high-resolution blended real-time global sea surface temperature analysis. *Bull Am Meteorol Soc* 84:645–656
- Vilibić I (2005) Numerical study of the Middle Adriatic coastal waters' sensitivity to the various air pressure travelling disturbances. *Ann Geophys* 23(12):3569–3578
- Vilibić I, Šepić J (2017) Global mapping of nonseismic sea level oscillations at tsunami timescales. *Sci Rep* 7:40818
- Ye X, Anderson EJ, Chu PY, Huang C, Xue P (2018) Impact of water mixing and ice formation on the warming of Lake Superior: a model-guided mechanism study. *Limnol Oceanogr* 64:558–574